https://doi.org/10.5194/egusphere-2026-2290
Preprint. Discussion started: 5 May 2026

Comprehensive validation of MODIS atmospheric temperature profile data across mainland China using sounding observations

Wenjie Zhang[1,2], Mengxi Qu[1], Ranhao Sun[2], Jiarui Zhao[1], Guicai Ning[3], Aziz Inamov[4], Zokhid Mamatkulovd[4], Di Zhou[5], Bakhtiyor Pulatov[6], Yuanjian Yang[1,3]*

1 State Key Laboratory of Climate System Prediction and Risk Management, Nanjing University of Information Science and Technology, Nanjing 210044, China.
2 State Key Laboratory of Regional and Urban Ecology.
3 School of Atmospheric Physics, Nanjing University of Information Science and Technology, Nanjing 21004, China.
4 Tashkent Institute of Irrigation and Agricultural Mechanization Engineers, Tashkent 100043, Uzbekistan.
5 State Key Laboratory of Integrated Service Networks, Xidian University, Xi'an 710071, China.
6 Central Asian University of Environmental and Climate Change Studies, Tashkent, Uzbekistan.

* *Correspondence to:* Yang Yuanjian (yyj1985@nuist.edu.cn)

Abstract. The vertical profile of atmospheric temperature is crucial for understanding energy transfer within the climate system. The Moderate Resolution Imaging Spectroradiometer (MODIS) atmospheric profile product (MOD07_L2) provides vertical temperature profiles at 5 km spatial resolution. However, comprehensive validation of its absolute accuracy—particularly for lower tropospheric stability (LTS) and temperature inversion layer (TIL) detection—remains limited. Therefore, this study conducted systematic evaluations using sounding data from 74 stations across mainland China spanning 2003–2020, encompassing both daytime and nighttime periods. Results indicated that absolute retrieval accuracy was generally superior at nighttime compared to daytime, with MOD07_L2 demonstrating better performance in upper layers (400–620 hPa) than in lower layers (850–1000 hPa). Nonetheless, retrieval errors at the 700 hPa level exhibited a more pronounced bias (B) relative to other pressure levels. In contrast, LTS accuracy was higher during daytime (r = 0.74, B = 0.04°C, RMSE = 4.52°C) than at nighttime (r = 0.57, B = 0.3°C, RMSE = 6.78°C).For TIL, MOD07_L2 displayed limited detection capability, achieving an overall detection rate of 6.6% during daytime and 13.1% at nighttime. This study provides essential data support for atmospheric science, hydrology, and ecology fields that rely on high-resolution vertical temperature profiles.

Keywords: MODIS, Vertical atmospheric temperature profiles, Absolute accuracy, Lower tropospheric stability, Temperature inversion layers

1 Introduction

The vertical distribution of atmospheric temperature constitutes a fundamental component of Earth's climate system, profoundly influencing weather patterns, atmospheric circulation, and surface environmental processes. In recent years, intensified global climate change has induced substantial alterations in this distribution. Notably, the pronounced tropospheric

https://doi.org/10.5194/egusphere-2026-2290
Preprint. Discussion started: 5 May 2026

warming juxtaposed against stratospheric cooling highlights the intricate energy exchanges and dynamic interactions among atmospheric layers (Dessler & Davis, 2010; Seidel et al., 2016). These anomalous variations in temperature profiles have consequently reconfigured global circulation patterns and heightened the frequency of extreme weather events (Seeley, 2021; Galfi et al., 2021).

In recent years, rapid advancements in remote sensing technology and numerical simulations have greatly advanced the observation and analysis of vertical temperature distributions from the surface to the stratosphere (Santer et al., 2018; Thorne et al., 2016). The acquisition of vertical temperature data drawn from diverse sources, yet notable disparities existed among datasets in spatial and temporal resolution, parameter coverage, and applicability. Reanalysis datasets, such as the National Centers for Environmental Prediction (NCEP), European Centre for Medium-Range Weather Forecasts Reanalysis 5 (ERA5), and Climatic Research Unit (CRU), offered global coverage and long-term consistency but fell short in meeting the demands of fields requiring high-resolution data (Hersbach et al., 2020; Gelaro et al., 2017; Saha et al., 2010). For instance, despite optimizations in NCEP's boundary layer parameterization, its coarse spatial resolution (2.5°) remained inadequate for resolving local-scale temperature details (Saha et al., 2010; Grimmond et al., 2010). Similarly, while the CRU dataset provided long-term records, its 0.5° resolution constrained its utility in local-scale studies (Harris et al., 2020). Furthermore, although ERA5 excelled in global climate trend analysis, its 0.25° resolution still imposed limitations on regional-scale investigations (Zhao et al., 2014). In contrast, the Moderate Resolution Imaging Spectroradiometer (MODIS) atmospheric profile product (MOD07_L2) emerged as an optimal choice for regional studies, owing to its high spatial resolution of 5 km (Schwarz et al., 2011; Chen et al., 2019). However, existing research has primarily focused on the retrieval accuracy of near-surface (2 m) air temperatures, with systematic evaluations of vertical profiles in mid-to-upper atmospheric layers largely absent (Zhang et al., 2021; Yuan et al., 2023). Additionally, some studies have employed MOD07_L2 vertical temperature profiles to examine atmospheric structures and thermal stratification, albeit relying on limited station data (Huang et al., 2020; Barlow et al., 2015). To date, no nationwide assessment of these profiles has been undertaken across complex terrains and diverse climatic zones.

Lower tropospheric stability (LTS) served as a pivotal factor influencing atmospheric vertical distributions and weather patterns, governing air vertical mixing and convective activity intensity. Variations in LTS exhibited strong correlations with atmospheric temperature profiles, particularly in modulating extreme weather events such as severe pollution episodes, air humidity fluctuations, and precipitation extremes (Ning et al., 2018; Guo et al., 2016a; Guo et al., 2016b). Additionally, Li et al. (2014) confirmed that in low-latitude oceanic regions, enhanced LTS is typically significantly associated with subsidence at 700 hPa and increased low-level cloud cover, indicating that LTS serves as a crucial link connecting large-scale dynamical processes with the vertical structure of clouds. As a high-resolution atmospheric vertical profile product, MOD07_L2 held substantial potential for national-scale LTS analysis, yet its efficacy in this domain remained unvalidated. In addition,

https://doi.org/10.5194/egusphere-2026-2290
Preprint. Discussion started: 5 May 2026

temperature inversion layers (TIL) represented a key feature of atmospheric vertical temperature distributions, suppressing vertical air mixing and thereby altering local climate conditions (Barlow et al., 2015; Li et al., 2019). Recent research further revealed a close coupling between the inversion layer and the atmospheric boundary layer, jointly influencing the vertical distribution and capture efficiency of aerosols (Liu et al., 2022). The MOD07_L2 dataset furnished temperature data across 20 vertical pressure levels, laying a robust foundation for inversion layer detection and analysis (Coll et al., 2012; Leng et al., 2019). Existing validations have predominantly relied on radiosonde or lidar data, leaving the performance of MOD07_L2 in inversion detection unevaluated on a systematic basis.

Therefore, this study makes several novel contributions to the field. First, it provides the first long-term (2003–2020) and nationwide validation of MOD07_L2 vertical temperature profiles across China's diverse climatic and topographic regions beyond previous site-specific assessments. Second, it represents the first systematic evaluation of the MOD07_L2 product's capability to retrieve LTS and detect TIL, thereby extending validation beyond single-level temperatures to derived parameters critical for boundary layer and climate studies. Third, the diagnostic analysis of retrieval errors—particularly the attribution of the 700 hPa bias to a combination of atmospheric dynamics, topographic effects, and sensor characteristics—provides actionable insights for both users of the MODIS archive and developers of future satellite missions.

2 Materials and methodology

2.1 Study area

This study covered the entirety of China, characterized by complex and diverse geographical and climatic conditions. China's topography ascended progressively from east to west, featuring low-lying plains and hills in the east and towering mountains and plateaus in the west—most notably the Tibetan Plateau, with an average elevation surpassing 4,000 m. This configuration established a pronounced topographical gradient. China encompassed a broad spectrum of climate types, spanning tropical zones in the south to cold temperate regions in the north, complemented by alpine climates in the west, thereby engendering substantial climatic diversity. Eastern coastal areas are predominantly humid, whereas western regions are largely arid or semi-arid. These geographical and climatic characteristics amplified variations in surface temperature distributions and atmospheric boundary layer features across regions. To delineate these regional distinctions more precisely, this study adopted China's agricultural zoning framework (Fig. 1), comprising the Northeast China Plain (NEP), the Northern Arid and Semi-Arid Region (NAS), the Huang-Huai-Hai Plain (HHH), the Loess Plateau (LP), the Qinghai-Tibet Plateau (TP), the Middle-Lower Yangtze Plain (MYP), the Sichuan Basin and Surrounding Areas (SB), the Yunnan-Guizhou Plateau (YGP), and Southern China (SC). This zoning scheme is accessible via the following link: https://gitcode.com/open-source-

https://doi.org/10.5194/egusphere-2026-2290
Preprint. Discussion started: 5 May 2026

toolkit/6b76d/commit/aab463c56bfbcb7b0de5024ef53da43a634529ac?ref=main.

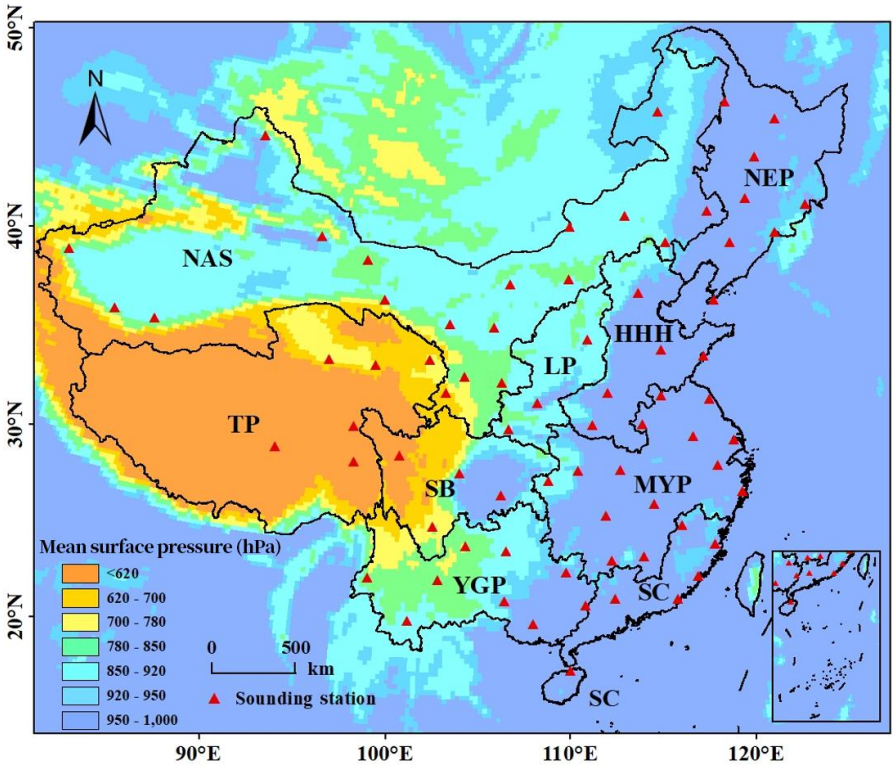

Figure 1. Annual mean surface pressure and sounding stations distribution in China from 2003 to 2020.

2.2 Data

2.2.1 Sounding data

The sounding data utilized in this study were provided by the China Meteorological Administration (http://weather.uwyo.edu/upperair/sounding.html). This investigation employed vertical temperature profile data from 74 stations recorded from 2003 to 2020 across China. These data were collected using meteorological balloons that measure atmospheric temperature, pressure, and other parameters at various altitudes, ranging from the surface to the upper atmosphere. Sounding observations were conducted daily at 00:00 and 12:00 across more than 100 pressure levels, thereby enabling a detailed characterization of the vertical temperature distribution. The sounding data used in this study adhere to the World Meteorological Organization (WMO) Global Climate Observing System (GCOS) Upper-Air Network (GUAN) standards and underwent rigorous quality control procedures. During the study period, the data completeness rate across all selected stations

https://doi.org/10.5194/egusphere-2026-2290
Preprint. Discussion started: 5 May 2026

exceeded 90%, providing a reliable foundation for statistical analysis.

2.2.2 MOD07_L2 data

This study utilizes the MOD07_L2 Collection 6.1 atmospheric profile product generated by NASA's Moderate Resolution Imaging Spectroradiometer (MODIS) sensor. This version incorporates significant improvements in retrieval algorithms and cloud detection, (https://ladsweb.modaps.eosdis.nasa.gov/search/). This product provided vertical atmospheric temperature profiles at 20 pressure levels (5, 10, 20, 30, 50, 70, 100, 150, 200, 250, 300, 400, 500, 620, 700, 780, 850, 920, 950, and 1000 hPa) with a spatial resolution of 5 km. For this study, temperature data were selected at the 400, 500, 620, 700, 780, 850, 920, 950, and 1000 hPa levels, which can represented key temperature distribution characteristics, such as LTS and TIL. For clear expression, the nine pressure levels were categorized into lower layers (850, 920, 950, and 1000 hPa), middle layers (700 and 780 hPa), and upper layers (400, 500, and 620 hPa). This classification aligned with standard isobaric surfaces in meteorological studies and reflected the characteristic atmospheric processes at varying altitudes. Additionally, surface pressure data were extracted from the MOD07_L2 product. This dataset shares the same 5 km spatial resolution as the temperature profiles and will be used to calculate near-surface potential temperature for the assessment of lower tropospheric stability.

2.3 Methodology

2.3.1 Vertical interpolation of vertical temperature profiles

To ensure the comparability between MOD07_L2 retrieved temperature profiles and sounding observation data, vertical interpolation of pressure levels was carried out in this study. A linear interpolation method was employed to interpolate the sounding temperature data onto the corresponding pressure levels of MOD07_L2. If a pressure level P_{modis} in MOD07_L2 exactly matched a pressure level in the sounding data, the corresponding sounding temperature T_{sod} was directly used without interpolation. For pressure levels in MOD07_L2 (P_{modis}) that did not match any sounding pressure levels, the two adjacent pressure levels in the sounding data (P_{lower} and P_{upper}) and the corresponding temperatures (T_{lower} and T_{upper}) were searched to satisfy the following relationship:

$$P_{\mathrm{lower}} < P_{\mathrm{modis}} < P_{\mathrm{upper}} \quad (1)$$

Then, the vertical temperature lapse rate γ was calculated as follows:

$$\gamma = \frac{T_{\mathrm{upper}} - T_{\mathrm{lower}}}{P_{\mathrm{upper}} - P_{\mathrm{lower}}} \quad (2)$$

This value indicated the amount of temperature change corresponding to a unit change in pressure between adjacent sounding

https://doi.org/10.5194/egusphere-2026-2290
Preprint. Discussion started: 5 May 2026

layers. By applying the calculated lapse rate γ, the temperature at the MOD07_L2 pressure level (P_{modis}) was interpolated to obtain its equivalent sounding temperature value as below:

$$T_{\mathrm{modis}} = T_{\mathrm{lower}} + \frac{T_{\mathrm{upper}} - T_{\mathrm{lower}}}{P_{\mathrm{upper}} - P_{\mathrm{lower}}} \times (P_{\mathrm{modis}} - P_{\mathrm{lower}}) \quad (3)$$

When P_{modis} fell outside the maximum or minimum pressure levels of the sounding data, the following approach was used to handle boundary cases: If the pressure value corresponding to the MOD07_L2 pressure level (P_{modis}) was greater than the maximum pressure value (P_{max} corresponding to the lowest altitude) in the sounding data, interpolation was performed using the two sounding pressure levels with the highest pressure values, $P_{\mathrm{max-1}}$ and P_{max}. Similarly, if the pressure value of MOD07_L2 (P_{modis}) was less than the minimum pressure value (P_{min} corresponding to the highest altitude) in the sounding data, P_{min} and $P_{\mathrm{min+1}}$ were used.

2.3.2 Sensitivity analysis of temporal matching window

Sounding data are typically observed at 00:00 and 12:00 Beijing Time. However, due to the sun-synchronous orbit of the Terra satellite carrying MODIS, the overpass times of MOD07_L2 data exhibit spatial variations within China, with earlier overpass times in the eastern regions compared to the western regions. To ensure the comparability between satellite retrievals and sounding observations, and to assess the impact of time deviations on retrieval accuracy, this study conducted a time-matching sensitivity experiment. The time deviation ($|\Delta t|$) was divided into four intervals: 0–0.5 hours, 0.5–1 hour, 1–1.5 hours, and 1.5–2 hours. Statistical metrics between MOD07_L2 temperature retrieval values and sounding data were calculated within each interval to determine the optimal matching window. Detailed sensitivity analysis results are presented in the Results section of this article.2.3.3 Lower Tropospheric Stability Calculation

Lower tropospheric stability (LTS) was defined as the difference between the potential temperature at 700 hPa level and that near the surface (Guo et al., 2016a; Ning et al., 2018). To accurately obtain the near-surface temperature from MOD07_L2 data, a linear interpolation method was employed. Based on the two pressure levels closest to the surface and their corresponding temperature values, the temperature corresponding to the surface pressure was calculated. In the sounding data, the near-surface layer was defined as the lowest pressure level and its corresponding temperature in the raw data. Subsequently, the temperatures at 700 hPa level and near the surface were converted to potential temperatures using the standard formula. The calculation formula for potential temperature (θ) is as follows:

$$\theta = T\left(\frac{p_0}{p}\right)^{\frac{R}{c_p}} \quad (4)$$

In this formula, T is the temperature (K), p is the pressure, p_0 is the reference pressure (usually taken as 1000 hPa), R is the

https://doi.org/10.5194/egusphere-2026-2290
Preprint. Discussion started: 5 May 2026

gas constant for dry air (R usually taken as 287.05 J·kg⁻¹·K⁻¹), and c_p is the specific heat at constant pressure for dry air (c_p usually taken as 1004 J·kg⁻¹·K⁻¹). After obtaining the potential temperatures at the 700 hPa level and near the surface, LTS was calculated as their difference:

$$\mathrm{LTS} = \theta_{700\mathrm{hPa}} - \theta_{\mathrm{surface}} \tag{5}$$

LTS represents atmospheric stability, higher values indicate greater stability.

2.3.4 Temperature inversion layer detection

The identification of TIL was based on analyzing the vertical temperature differences between neighboring pressure levels. Under standard adiabatic conditions, temperature should decrease as pressure decreases. If adverse, temperature inversion was defined. To evaluate the detection accuracy of temperature inversions in the MOD07_L2 data, its results were compared against sounding observations. The number of inversion layers co-detected with the sounding data (N_{both}) was calculated. The ratio of this number to the total number of inversions independently detected by the soundings (N_{SD}) defines the inversion detection accuracy for that dataset:

$$A = \frac{N_{\mathrm{both}}}{N_{\mathrm{SD}}} \tag{6}$$

https://doi.org/10.5194/egusphere-2026-2290
Preprint. Discussion started: 5 May 2026

3 Results

3.1 Sensitivity analysis of time-matching window

To determine the optimal time-matching window, we analyzed the variations in accuracy between MOD07_L2 temperature retrievals and sounding observations under different time deviations ($|\Delta t|$) (Fig. 2). The results indicate that when $|\Delta t| < 1$ hour, no effective matches were found in the NEP, and the sample size in the HHH was also limited, making it insufficient to support a national-scale evaluation. When the window was expanded to 1–1.5 hours and 1.5–2 hours, the sample size increased significantly, but the B in some regions became larger: during daytime, the bias in HHH reached -1.77°C under the 1–1.5 hour window (Fig. 2C); at night, under the 1.5–2 hour window, the bias in the NEP reached 2.24°C, and in the NAS increased to -0.78°C (Fig. 2D). Nevertheless, the r at most sites remained above 0.9, and the increase in RMSE was within an acceptable range. Balancing sample coverage and retrieval accuracy, this study selected $|\Delta t| < 2$ hours as the final matching threshold. This threshold ensures sufficient sample size across the national scale while controlling the uncertainty introduced by temporal mismatch at a reasonable level, laying the foundation for subsequent validation of temperature profiles and derived parameters.

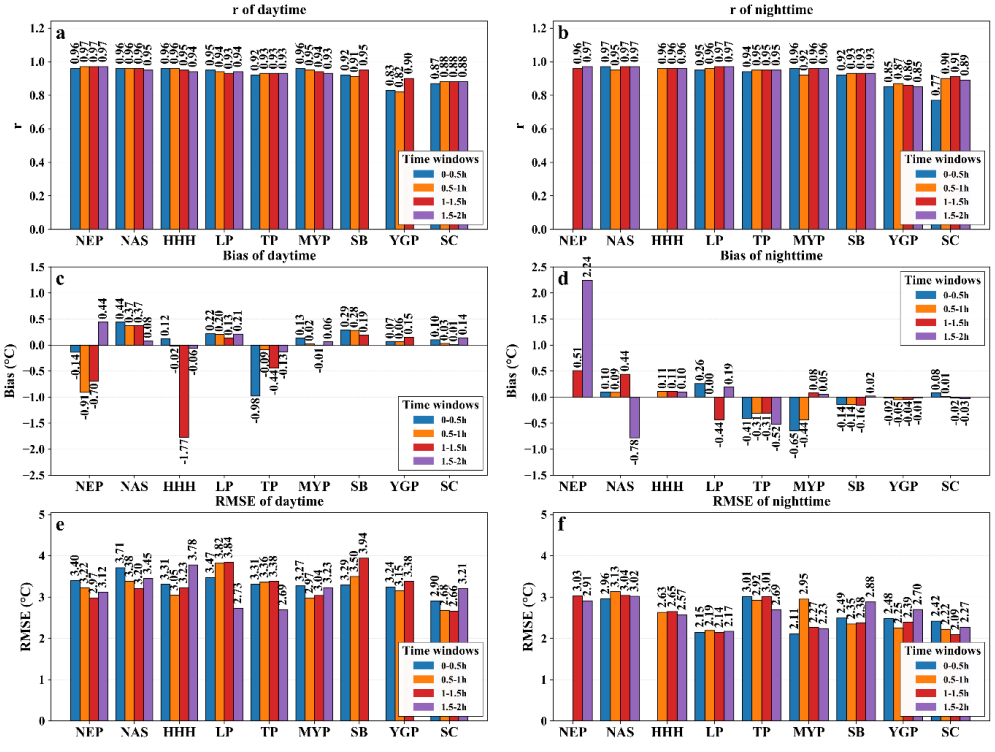

Figure 2. Sensitivity analysis of temperature retrieval accuracy to different temporal matching windows. (a), (c), and (e) show

https://doi.org/10.5194/egusphere-2026-2290
Preprint. Discussion started: 5 May 2026

daytime correlation coefficient (r), bias (B), and root mean square error (RMSE), respectively; (b), (d), and (f) show the corresponding nighttime statistics.

3.2 The overall absolute retrieval accuracy during daytime and nighttime

Figure 3 illustrated the density scatter distributions between MOD07_L2 instantaneous retrievals and sounding temperatures at different pressure levels during daytime. Results indicated that the retrieval accuracy of MOD07_L2 data was high in the upper layers (400, 500 , and 620 hPa). Specifically, at 400 hPa, the r was 0.95, the B was near 0°C, and the RMSE was around 2.8°C. Similar trends were observed at the 500 and 620 hPa levels, where the r remained above 0.95, the B approached 0°C, and the RMSE ranged from 2.5°C to 2.7°C. These results demonstrated the good consistency between the retrievals and the observations in the upper layers. However, the error increased in the lower layers (850, 920, 950 hPa and 1000 hPa). Particularly at the 920 hPa, the r was 0.96, the B was near 0.2°C, and the RMSE reached approximately 4.1°C. This indicated that the retrieval results of MOD07_L2 were unstable in the lower layers. In addition, the 700 hPa presented the high r of 0.97 and the RMSE of 2.69°C, but the B was 0.49°C, which was higher than that at other layers. Overall, MOD07_L2 exhibited better retrieval accuracy in the upper layers during daytime conditions, but retrieval errors were larger than those in the lower layers, especially near the surface.

https://doi.org/10.5194/egusphere-2026-2290
Preprint. Discussion started: 5 May 2026

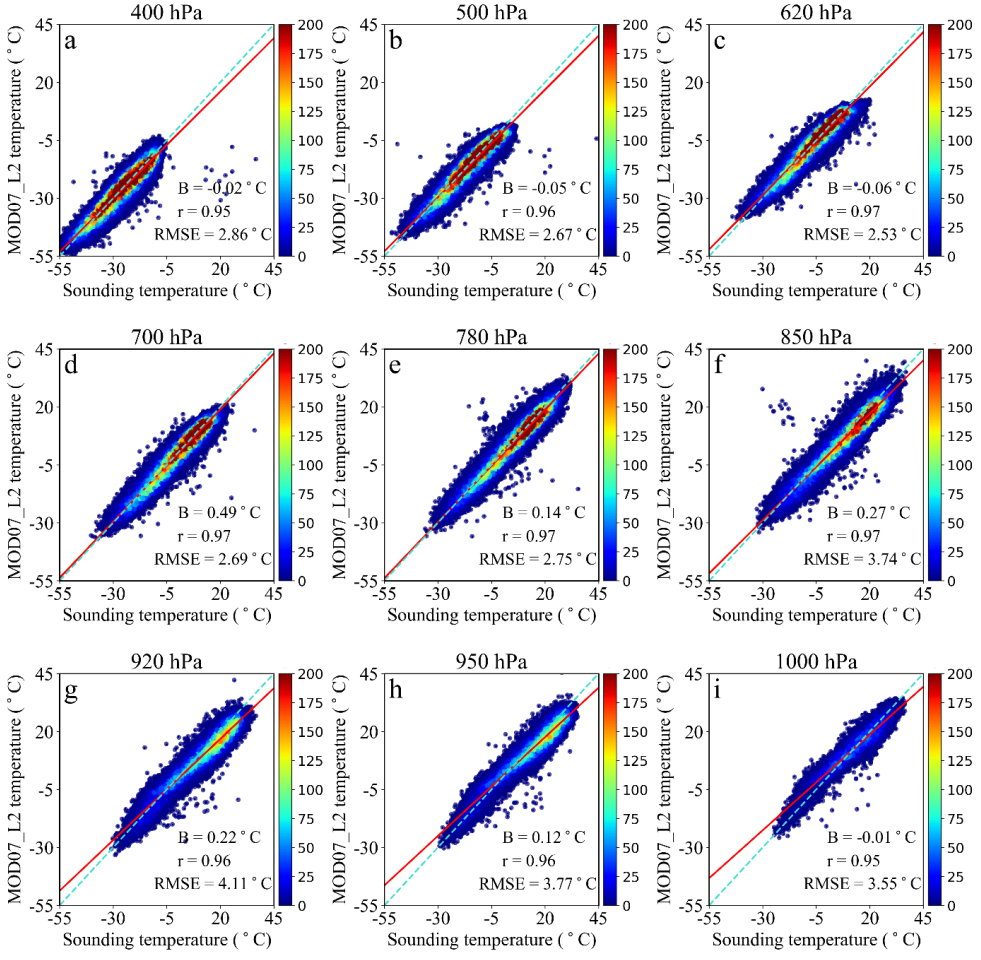

Figure 3. Overall accuracy of MOD07_L2 retrieved temperatures compared with sounding observed temperatures during daytime from 2003 to 2020.

Figure 4 illustrated the density scatter distributions between MOD07_L2 instantaneous retrieved and observed atmospheric temperatures during nighttime. In general, the overall retrieval performance during nighttime was better than that during daytime. In the upper layers, the r was above 0.96, the B approached 0°C, and the RMSE was ranged from 2.2°C to 2.7°C. However, at the 700 hPa, the nighttime retrieval B reached 0.56°C, which was higher than other levels. In the lower layers, the RMSE remained lower than during the daytime. For example, at the 1000 hPa, the r increased from 0.95 during daytime to 0.97, the B remained near 0°C, and the RMSE improved to approximately 2.6°C.

https://doi.org/10.5194/egusphere-2026-2290
Preprint. Discussion started: 5 May 2026

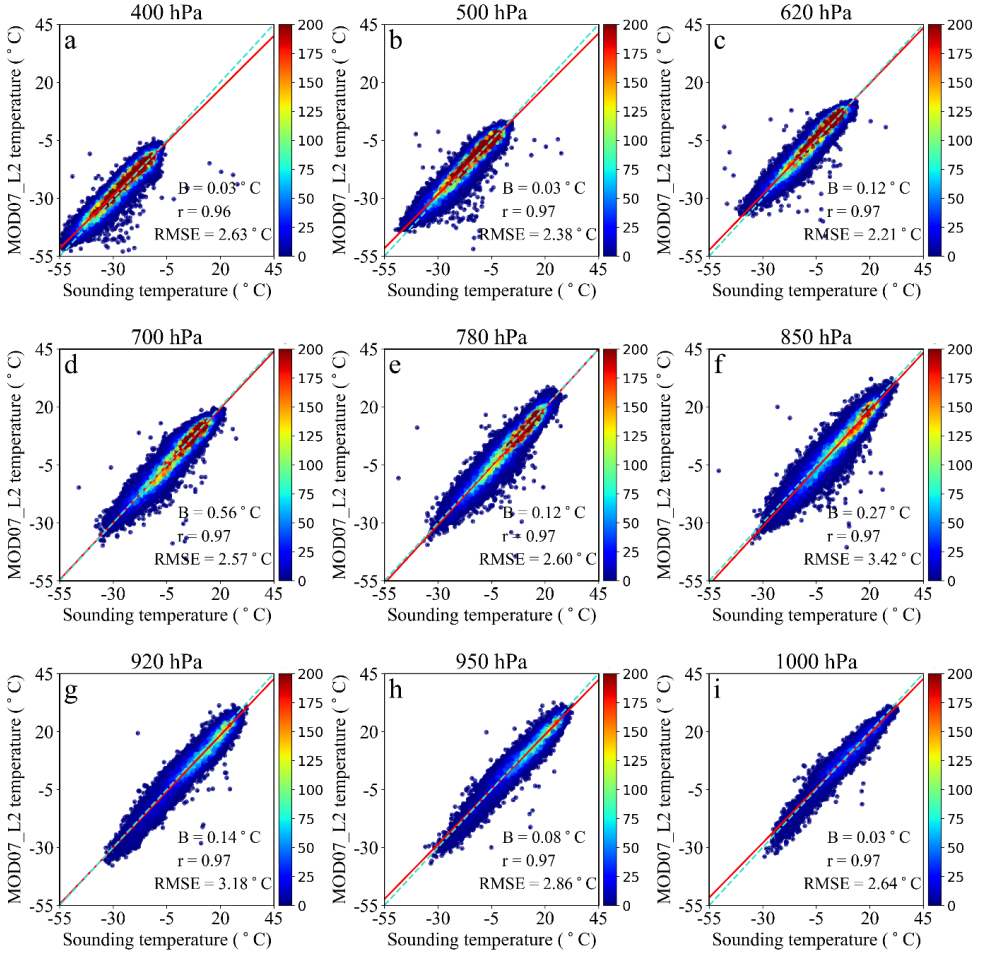

Figure 4. Overall accuracy of MOD07_L2 retrieved temperatures compared with sounding observed temperatures during nighttime from 2003 to 20203.3 The Spatial Distribution of the Absolute Retrieval Accuracy.

Figure 5 presents the spatial distribution of MOD07_L2 retrieval accuracy metrics across various pressure levels during daytime. The first two columns display the effective matching sample size for each station and the pressure difference (ΔP) between the given level and the near-surface layer, respectively. The sample size generally exhibits a decreasing trend from northwest to southeast across China. The spatial pattern of the ΔP reflects the influence of topography, where a smaller value indicates that the selected standard isobaric surface is closer to the local ground surface in those regions. The retrieval accuracy of MOD07_L2 varies across different regions and atmospheric pressure levels. In the upper layers, retrieval performance was optimal in regions characterized by flat terrain, ample sample sizes, and a large ΔP from the surface, such as the NEP, NAS, and HHH. The r exceeded 0.95, the B was within ±0.5°C, and the RMSE was around 2.5°C. Nevertheless, at some stations

https://doi.org/10.5194/egusphere-2026-2290
Preprint. Discussion started: 5 May 2026

over the TP and the MYP, the RMSE at these pressure levels increased to approximately 3.0°C. In the middle levels, the retrieval accuracy improved over the MYP and SB compared with the upper layers. Conversely, in the lower layers, the retrieval errors increased. Particularly over the SC, MYP, and YGP, where sample sizes are relatively small, despite favorable r and minimal B, the RMSE was above 3.5°C. In contrast, retrievals over the NEP and the HHH at the lower layers indicated better accuracy, with r greater than 0.9, the B near 0°C, and the RMSE stabilized near 3.0°C. Overall, under daytime conditions, MOD07_L2 exhibited superior retrieval accuracy at upper-air pressure levels, particularly over flat terrain. In contrast, larger retrieval errors were observed in the lower pressure layers, over complex terrain, and across southern regions with limited data availability.

https://doi.org/10.5194/egusphere-2026-2290
Preprint. Discussion started: 5 May 2026

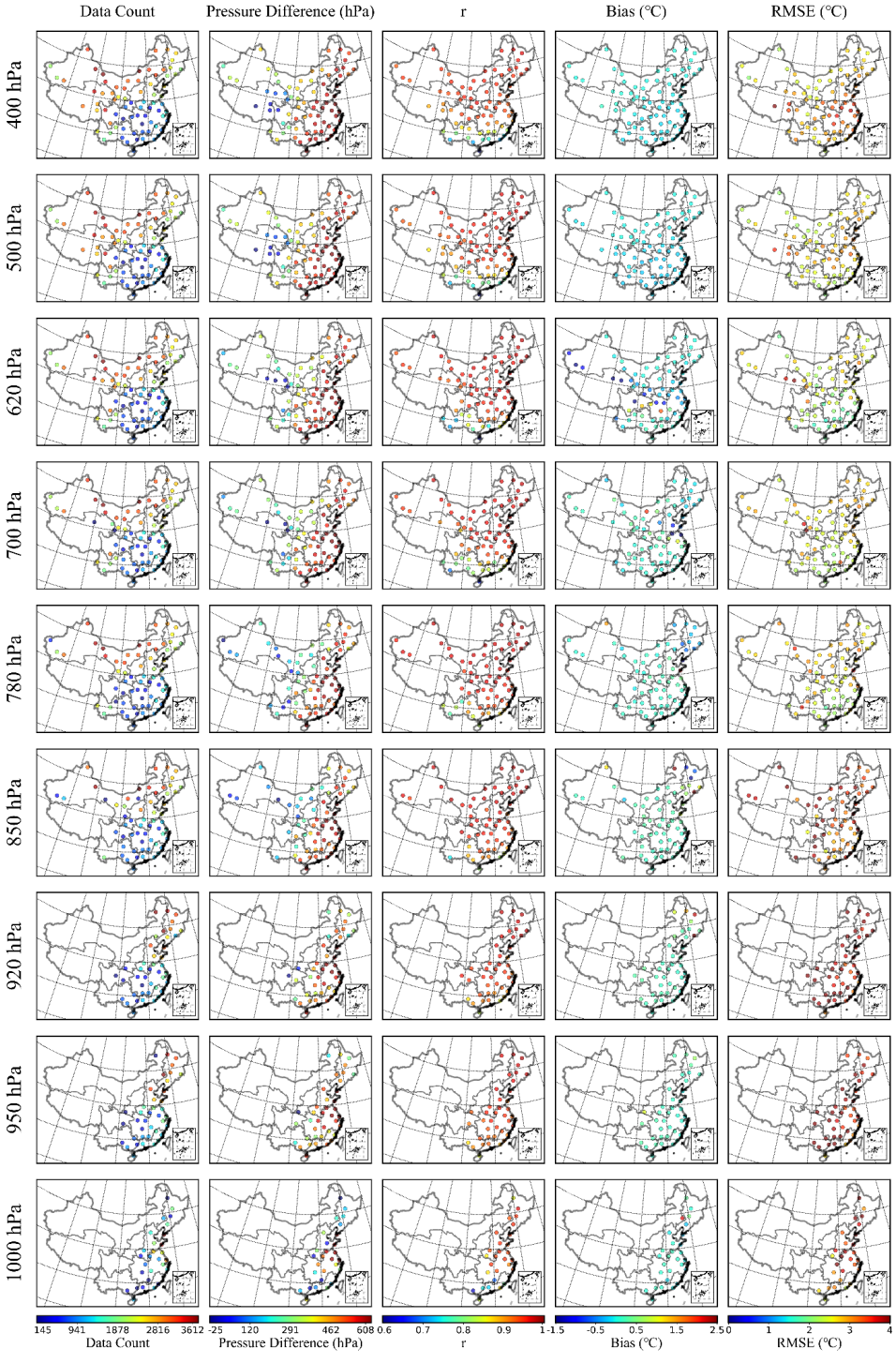

Figure 5. Spatial distribution of statistical indicators at each station for MOD07_L2 retrieved versus sounding temperatures at nine

https://doi.org/10.5194/egusphere-2026-2290
Preprint. Discussion started: 5 May 2026

pressure levels during daytime from 2003 to 2020.

Figure 6 illustrated the comparison between MOD07_L2 retrieved temperatures and sounding observations at different pressure levels during nighttime. The first two columns present the effective matched sample size for each station and the ΔP between the given atmospheric level and the near-surface layer, respectively. Spatially, the nighttime sample size exhibits a decreasing gradient from northeast to southwest in the upper and middle layers, while lower counts are observed in the lower layers over the NEP, SC, and the southeastern part of the YGP. Overall, the retrieval accuracy was higher during nighttime than during daytime. In the upper layers, the retrieval accuracy was slightly higher than daytime accuracy over flat regions such as the NEP, HHH, and NAS. The r was above 0.95, the B was close to 0°C, and the RMSE at most stations fell between 2.0°C and 2.5°C. In particular, the RMSE decreased by about 0.5°C compared to daytime over the TP and MYP regions. In the middle layers, nighttime retrieval errors were generally lower than those during the daytime. Overall, the r remained above 0.95, and the B was close to 0°C. Regionally, the RMSE was about 2.5°C over the NEP and HHH, and about 3.0°C over the NAS. All of these were lower than their daytime counterparts. In the lower layers, the retrieval accuracy at nighttime showed improvement, especially in over the HHH and MYP. The r approached 0.9 and the B remained near 0°C at these regions and the RMSE decreased to around 2.0°C. However, in the NEP region, where the sample size was relatively small, considerable retrieval errors persisted in the lower atmospheric layers, where r decreased to around 0.9, the B exceeded ±0.5°C, and the RMSE ranged between 3.0°C and 4.0°C. In general, nighttime retrieval accuracy of MOD07_L2 was higher than that during daytime in the upper layers, especially over flat regions. In contrast, the retrieval errors exhibited only a slight increase in lower atmospheric levels, especially in regions characterized by both complex topography and data scarcity.

https://doi.org/10.5194/egusphere-2026-2290
Preprint. Discussion started: 5 May 2026

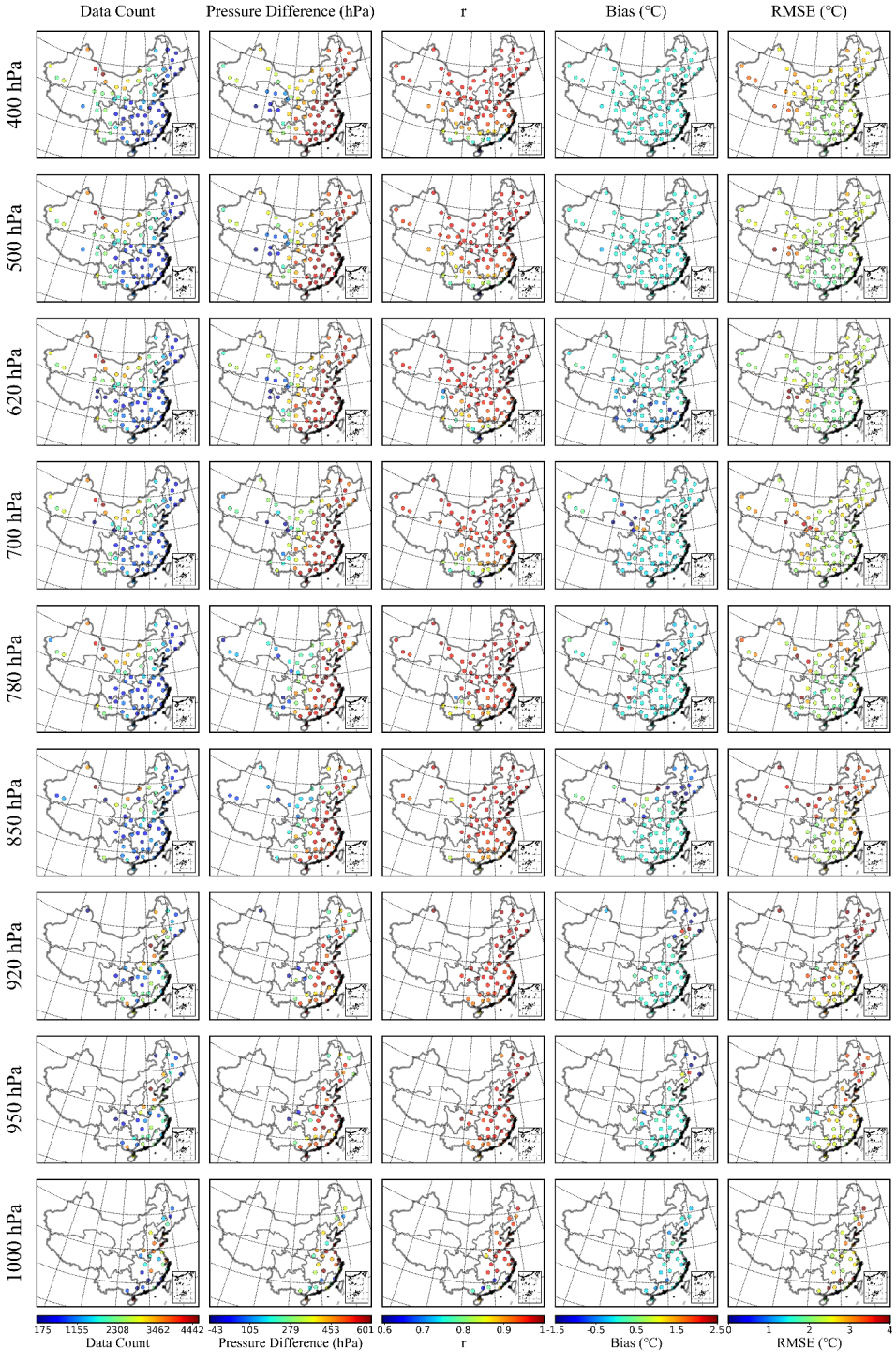

Figure 6. Spatial distribution of statistical indicators at each station for MOD07_L2 retrieved versus sounding temperatures at nine

https://doi.org/10.5194/egusphere-2026-2290
Preprint. Discussion started: 5 May 2026

pressure levels during nighttime from 2003 to 2020.

3.4 The accuracy of lower tropospheric stability

Figure 7 illustrated the ability of the MOD07_L2 product to capture lower tropospheric stability (LTS) during both daytime and nighttime. During daytime, the r, B, and RMSE were 0.74, 0.04 °C, and 4.52 °C, respectively. In contrast, during nighttime, r decreased to 0.57, the B increased to 0.30°C and the RMSE rose to 6.78°C. Furthermore, during nighttime, the red regression line diverged more substantially from the cyan diagonal in the density scatter plot, indicating a pronounced systematic error.

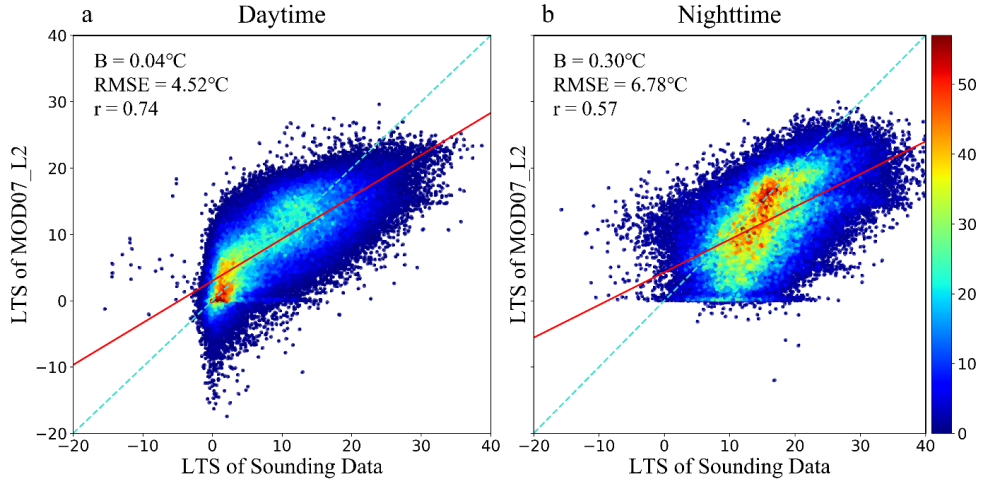

Figure 7. Heat map of lower tropospheric stability derived from sounding and MOD07_L2 observations during daytime and nighttime from 2003 to 2020.

In terms of spatial distribution, the retrieval accuracy of LTS exhibited pronounced regional variability during both daytime and nighttime. During daytime, r values were lower in humid and topographically complex regions such as the SB, MYP, LP, and HHH, with most values falling below 0.5. By contrast, the r values were higher in northern and southern regions, particularly over the NAS where the mean approached 0.6. These results indicated that retrieval performances were superior in arid and flat terrains. The mean RMSE during daytime was about 4°C nationwide, but that was lower along the margins of the TP. Additionally, the large mean biases were evident at the margins of the TP, indicating a systematic error in this area. In contrast, most other regions exhibited modest biases, with errors displaying patchy spatial variability. During nighttime, the spatial distribution of r exhibited a distinct pattern. On the NAS and along the margins of the TP, the r fell below 0.6. In contrast, the higher r values were observed over southeastern and northeastern China, suggesting that retrieval performance in humid zones improved at nighttime compared with daytime. Nighttime RMSE values were lower over the YGP, SC, MYP, and HHH,

https://doi.org/10.5194/egusphere-2026-2290
Preprint. Discussion started: 5 May 2026

268 mostly ranging from 3°C to 4°C, reflecting greater retrieval stability. The RMSE values were elevated over eastern and
269 southern China, as well as along the TP margins, generally exceeding 5°C and thereby indicating greater uncertainty. In terms
270 of bias, eastern and southern China exhibited small deviations, whereas systematic biases persisted on arid and high-elevation
271 regions.

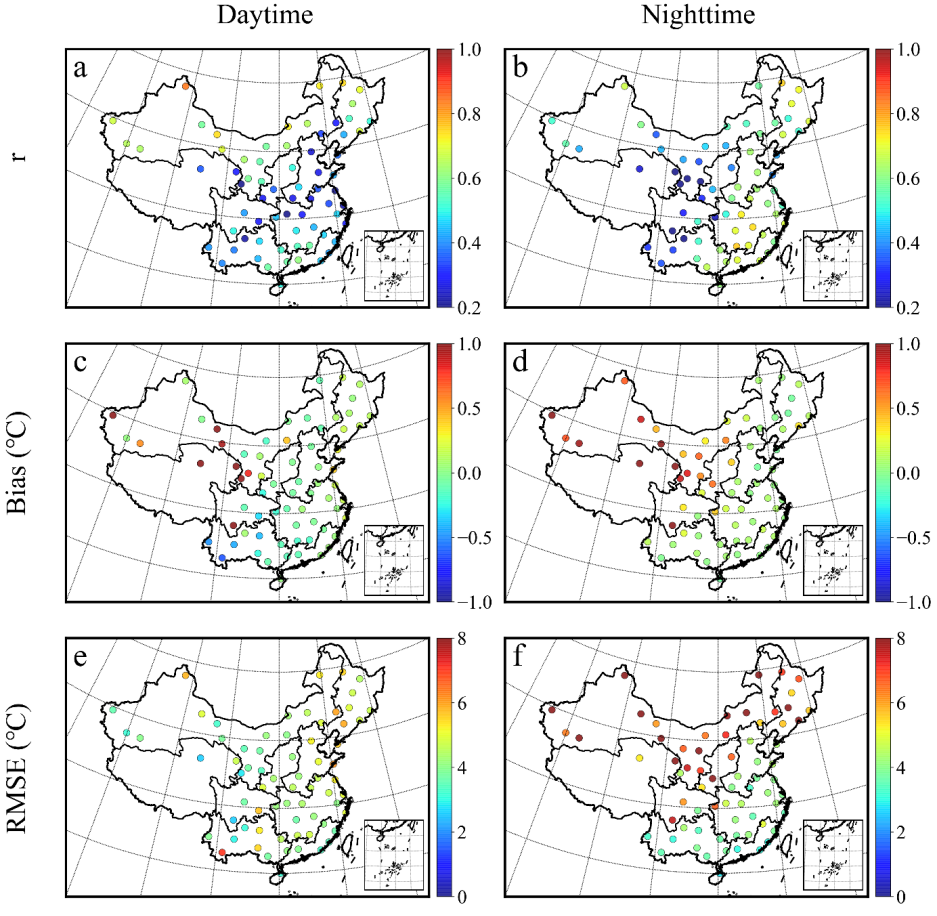

272

273 **Figure 8. Spatial distribution of MOD07_L2 lower tropospheric stability retrieval accuracy for daytime and nighttime from 2003 to**
274 **2020. (a), (c), and (e) show daytime r, B, and RMSE, respectively; (b), (d), and (f) show the corresponding nighttime metrics.**

275 **3.5 The identification of temperature inversion layers**

276 Figure 9 illustrated the detection results of TILs by MOD07_L2 over China and its nine agricultural zones during daytime and
277 nighttime. Overall, the proportion of TILs detected by MOD07_L2 was low, with 6.6% during daytime and 13.1% during
278 nighttime. Generally, regions with higher detection rates during the daytime also exhibited higher rates during the nighttime,

https://doi.org/10.5194/egusphere-2026-2290
Preprint. Discussion started: 5 May 2026

except for the SB. During the daytime, the detection rate of inversion layers by MOD07_L2 was below 6% in most regions, even no inversion layers were detected on the TP and in the SB. Only NAS and NEP showed respective 10.6% and 8.4% detection rates during daytime. During nighttime, the detection rate remained below 10% in most regions, with only NEP and NAS at 29.9% and 20.0%, respectively. No inversion layers were detected on the TP during nighttime. In general, the detection rates were higher during nighttime than during daytime across most regions.

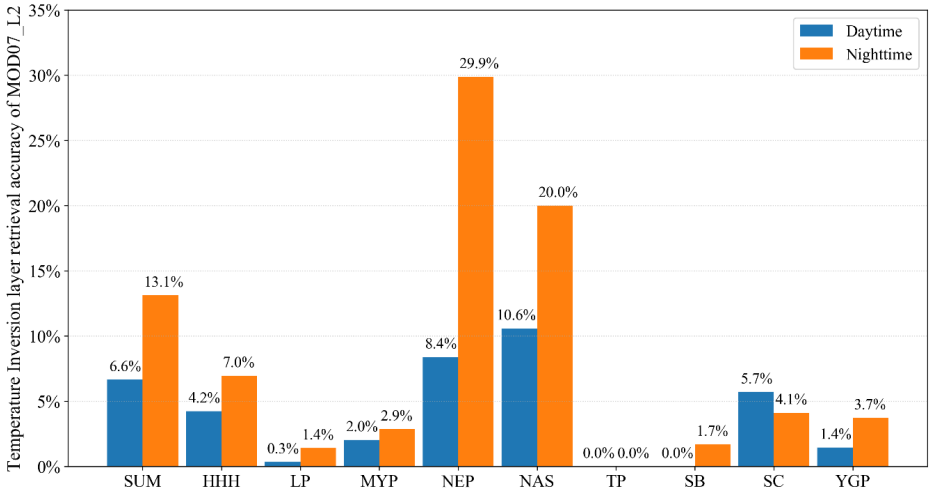

Figure 9. The overall detection accuracy of MOD07_L2 for temperature inversion layers, as well as over nine agricultural regions during daytime and nighttime.

As illustrated in Fig. 10, the spatial distributions and detection accuracies of temperature inversions derived from sounding data and MOD07_L2 exhibited marked discrepancies between daytime and nighttime. During daytime, sounding data recorded the highest inversion counts in the NEP, with two stations surpassing 1000 events. Most stations in the NEP and HHH region ranged from 200 to 500 counts, while those in other areas were predominantly below 200. Notably, two stations on the TP detected no inversions. In contrast, MOD07_L2 identified inversion counts between 50 and 500 solely in the northern portions of the NEP and in the NAS. The majority of stations elsewhere fell below 50 counts and no detections were detected in the SB. Only one northeastern station on the TP detected a minimal number. Furthermore, stations in the western portions of the YGP and on the MYP also failed to detect any inversions. Detection precision exceeded 10% at only a few isolated sites in the northern in the northern NAS and NEP regions. During nighttime, sounding data revealed that inversion events were more prevalent and frequent. Stations with inversion counts exceeding 1000 were primarily distributed in western NAS, northern LP, and northern HHH. Specifically, inversion counts in western NAS, NEP, HHH, and LP were relatively high, all surpassing

https://doi.org/10.5194/egusphere-2026-2290
Preprint. Discussion started: 5 May 2026

200. In contrast, the TP exhibited the fewest inversions, with two stations detecting none. The detection performance of MOD07_L2 improved at night, identifying 500–1000 inversions at three stations in northern NAS and exceeding 50 counts in NEP, northern NAS, and northern HHH. However, inversion counts at stations in other regions remained below 50. Detection precision reached 10% only in northern NAS and northern NEP. Notably, MOD07_L2 failed to detect any inversions at stations on the TP, as well as in parts of the SB and MYP.

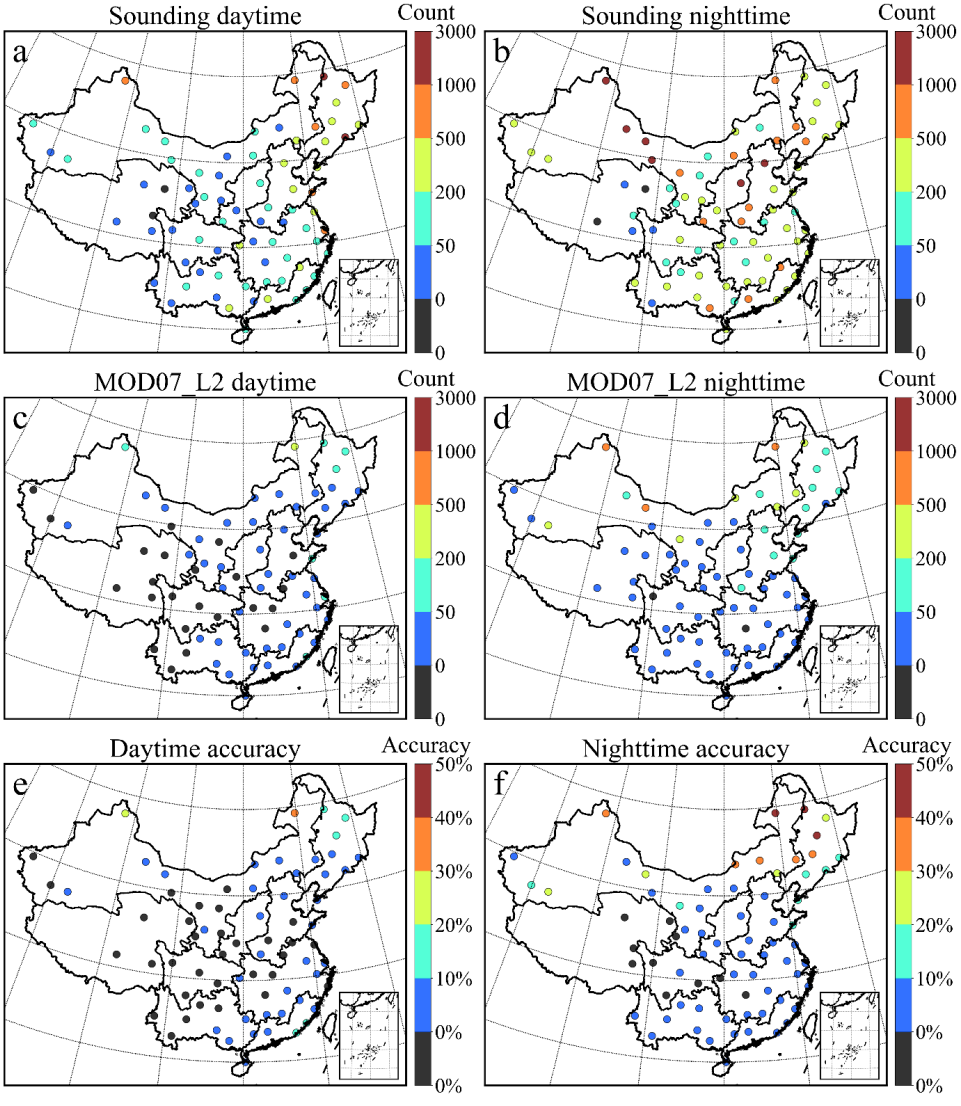

Figure 10. Spatial distribution and precision of temperature inversion detection based on MOD07_L2 and sounding data during daytime and nighttime from 2003 to 2020. (a) and (b) show the daytime and nighttime distributions derived from sounding data, (c)

https://doi.org/10.5194/egusphere-2026-2290
Preprint. Discussion started: 5 May 2026

and (d) show the corresponding distributions from MOD07_L2, (e) and (f) show the detection precision at each station for daytime and nighttime.

4 Discussion

4.1 Uncertainty of the absolute temperature retrieval

This study reveals that the retrieval accuracy of MOD07_L2 satellite temperature profiles significantly decreases as pressure levels approach the Earth's surface. This phenomenon primarily arises from stronger interference by surface longwave radiation in the lower atmosphere, greater variability in surface thermal inertia, and more intense local circulation and temperature fluctuations induced by complex terrain near the surface (Xue et al., 2023; Cheng et al., 2025; Song et al., 2024). Retrieval accuracy is higher in the upper layers. whereas errors increase in the lower layers, with the largest errors occurring in levels close to the surface. Additionally, overall retrieval accuracy is higher at night than during the daytime, mainly because nighttime surface radiative cooling reduces diurnal variations in thermal infrared signals (He et al., 2023).

Spatially, the retrieval errors exhibit pronounced regional heterogeneity. In the TP, errors in the middle and lower layers are high, primarily attributable to high elevation and complex terrain causing standard pressure levels to be closer to the surface, as well as extreme diurnal temperature variations that amplify fluctuations in thermal infrared signals (Zhao et al., 2020; Ma et al., 2023). Additionally, the MOD07_L2 product integrates multi-channel infrared brightness temperatures with global reanalysis and sounding data through statistical regression and physical retrieval algorithms (Sobrino et al., 2014; Zhang et al., 2025). In high-elevation regions, the limited number of meteorological stations and sounding observations increases errors in numerical simulations (Zhang et al., 2023). The SB and MYP, experience significantly larger lower-layer errors due to humid climate, frequent stratiform cloud cover, and topographic enclosure (Zhang et al., 2019; Feng et al., 2020). In the NAS, sparse vegetation cover weakens near-surface energy exchange, thereby increasing retrieval errors in the lower layers (Meier et al., 2022). Dust storms and aerosols with high optical thickness further interfere with atmospheric transmittance (Huang et al., 2020).

It is particularly noteworthy that MOD07_L2 exhibits substantial systematic biases at the 700 hPa level. The causes of this bias are complex. First, the 700 hPa level serves as a key interface in the mid-troposphere, commonly used to characterize mid-level humidity, vertical motion, and weather system structures such as fronts and shear lines. Its temperature field displays strong spatial heterogeneity, making retrieval or assimilation challenging (Hersbach et al., 2020; Li et al., 2021). Second, in high-elevation regions of China, the 700 hPa standard pressure level lies closer to the surface, rendering this layer susceptible to contamination by surface influences during retrieval (Ma et al., 2023; Zhao et al., 2020). Additionally, the weighting

https://doi.org/10.5194/egusphere-2026-2290
Preprint. Discussion started: 5 May 2026

functions of MODIS infrared channels typically peak near the 700 hPa level in the mid-troposphere. This makes them sensitive to temperature but highly susceptible to interference from clouds, water vapor, and aerosols, resulting in cloud contamination or weakened signals in absorption bands (Menzel et al., 2019; Platnick et al., 2003).

4.2 Uncertainty of lower tropospheric stability and temperature inversion layer

This study revealed that the accuracy of LTS retrieved by MOD07_L2 was higher during the daytime than at nighttime, which appears inconsistent with the superior absolute retrieval accuracy of atmospheric temperature observed at night. This discrepancy arose from the nature of LTS as a derived parameter, whose accuracy hinges not only on the absolute retrieval precision of individual layer temperatures but also on the fidelity of vertical temperature gradient retrieval. At night, although atmospheric temperature retrieval accuracy may be enhanced, the frequent occurrence of strong near-surface inversion layers heightened vertical structural complexity (Kaushal et al., 2022; Tan et al., 2021). Furthermore, clouds further complicate nighttime boundary layer structure. A ground-based study at the Southern Great Plains site showed that during cloudy nights, clouds absorb surface longwave radiation and re-radiate it downward, reducing surface radiative cooling rates and thereby enhancing atmospheric instability and turbulence intensity (Liu et al., 2025). This leads to more complex vertical temperature gradients at night, increasing the difficulty of LTS retrieval using MOD07_L2. The limited vertical resolution of MOD07_L2 thus struggled to resolve sharp temperature gradients within thin inversion layers, leading to underestimation of near-surface potential temperature via linear interpolation. Moreover, nighttime thermal infrared remote sensing exhibited diminished sensitivity to subtle thermal variations in the boundary layer (He et al., 2023). In humid regions such as SB and MYP, prevalent cloud cover and elevated water vapor further attenuate infrared signal sensitivity to the lower atmosphere (Zhang et al., 2019), thereby degrading LTS retrieval accuracy. Additionally, in areas like the TP edges and NAS, intense nighttime radiative cooling induced rapid temperature gradient shifts, exacerbating LTS retrieval errors (Tian et al., 2023; Chen et al., 2022).

In addition, MOD07_L2 identified only a limited number of TILs, possibly due to its 5 km spatial resolution, which may average out thin inversion structures (Seemann et al., 2016). Furthermore, the limited vertical sampling of only 20 standard pressure levels in MOD07_L2 hindered the resolution of shallow near-surface inversions. MOD07_L2 data indicated that nighttime inversions were more frequent than those during the daytime, attributable to nighttime surface longwave cooling that readily initiates and sustains near-surface inversions. This mechanism aligned with findings from multi-site radiosonde observations (Zhang et al., 2022; Zeng et al., 2022). The present study further demonstrates that MOD07_L2 exhibited a higher detection rate and accuracy for nighttime inversions compared to daytime ones, primarily owing to the enhanced boundary layer stability and reduced atmospheric turbulence, which improve the reliability of satellite-based inversion detection (Tan et al., 2021). On a regional scale, the frequency of temperature inversion detection over the Tibetan Plateau is relatively low. This

https://doi.org/10.5194/egusphere-2026-2290
Preprint. Discussion started: 5 May 2026

finding aligns with recent evaluations of reanalysis products over the TP, which have also revealed substantial challenges in capturing low-level temperature inversions due to complex terrain and surface–atmosphere interactions (Luo et al., 2025). Furthermore, MOD07_L2 provided fewer effective pressure levels at high-altitude regions, thereby reducing its inversion detection capabilities (Che et al., 2021; Chen et al., 2016). At the SB, the humid and enclosed terrain promoted inversion formation. However, the multi-layered structure and moist air impeded thermal infrared profile retrieval, resulting in lower accuracy (Feng et al., 2020; Feng et al., 2023). At high latitude areas, despite the greater temporal mismatch between the datasets at northern NEP and NAS, MOD07_L2 demonstrated superior accuracy in inversion layer detection in these regions. This finding aligned with long-term radiosonde climatology, underscoring that colder, higher-latitude areas were prone to forming thicker and stronger near-surface inversions (Guo et al., 2020). In humid southern regions such as MYP and YGP, abundant moisture and thin inversion layers impeded effective detection by MOD07_L2. Furthermore, Huang et al. (2021) reported that humid southern China predominantly featured thin, weak elevated inversions, which posed significant challenges for reliable infrared profile retrievals.

4.3 Future effort

Based on the systematic validation of the high-resolution MOD07_L2 satellite product conducted in this study, the performance characteristics and regional applicability of this dataset in terms of vertical temperature profile absolute accuracy, lower tropospheric stability (LTS), and temperature inversion layer (TIL) detection have been clarified. Future work can be deepened in the following directions. First, optimize the spatiotemporal matching scheme by developing more refined interpolation methods or incorporating atmospheric model corrections to reduce boundary layer evolution errors potentially introduced by the $|\Delta t| < 2$-hour window. Second, deepen error attribution analysis by integrating auxiliary data such as cloud cover, aerosol optical depth, water vapor, and terrain, combined with radiative transfer simulations or machine learning methods, to quantitatively diagnose the formation mechanisms of systematic biases at 700 hPa and regional differences. Finally, further improve the retrieval algorithm performance of the MOD07_L2 product and explore feasible pathways for integrating multi-source observational data, with the aim of generating higher-accuracy temperature profile products, thereby significantly enhancing their application value in regional high-impact weather mechanism analysis, local climate monitoring, and environmental assessment.

5 Conclusion

While the MOD07_L2 atmospheric temperature profile product provides important information at high spatial resolution, there is still a lack of comprehensive evaluation in terms of its absolute retrieval accuracy and its capability to assess boundary layer

https://doi.org/10.5194/egusphere-2026-2290
Preprint. Discussion started: 5 May 2026

stability and detect temperature inversions. Therefore, we conducted a comprehensive assessment by comparing it with 74 geographically dispersed sounding stations from 2003 to 2020 across China. The absolute retrieval accuracy of MOD07_L2 showed clear differences across pressure layers during both daytime and nighttime, with nighttime accuracy generally better than that during daytime. Meanwhile, the upper layers (400–620 hPa) demonstrated higher accuracy, whereas the lower layers (850–1000 hPa) exhibited larger errors in humid and topographically complex regions. However, the retrieval errors at the 700 hPa level showed a more significant bias than those in other pressure levels. In contrast, the retrievals of lower tropospheric stability were more reliable during daytime than nighttime. Moreover, there were limitations in detecting temperature inversion layers during both daytime and nighttime. The findings of this study enhance the utility of MODIS's long-term data archive for climate applications and provide a valuable reference for the development and validation of similar products from current and future satellite missions, such as the VIIRS instrument.

CRediT authorship contribution statement

Zhang Wenjie: Conceptualization, Methodology, Supervision, Funding acquisition, Resources, Writing – review & editing. Qu Mengxi: Methodology, Supervision, Data curation, Formal analysis, Writing - Original Draft. Sun Ranhao and Zhao Jiarui: Validation, Supervision. Ning Guicai: Conceptualization, Investigation, Writing – review & editing. Aziz Inamov, Zokhid Mamatkulovd and Zhou Di: Validation, Methodology. Bakhtiyor Pulatov: Methodology. Yang Yuanjian: Conceptualization, Methodology, Supervision, Resources, Writing – review & editing.

Acknowledgments

This study is financially supported by the National Key Research and Development Program of China (2023YFE0208100), the National Natural Science Foundation of China (Grant 42201053 and 42222503) and the open fund project of the State Key Laboratory of Regional and Urban Ecology (Grant SKLURE2023-2-4).

Data availability

The shapefile data of agricultural zones is accessible from https://gitcode.com/open-source-toolkit/6b76d/commit/aab463c56bfbcb7b0de5024ef53da43a634529ac?ref=main. The MOD07_L2 data are available from https://doi.org/10.5067/MODIS/MOD07L2.061. The sounding data are available from http://weather.uwyo.edu/upperair/sounding.html. These data are openly accessible, and no permissions are required to download them. The corresponding data citations have been included in the reference list of this manuscript.

Declaration of competing interest

Some authors are members of the editorial board of *Atmospheric Measurement Techniques*.

https://doi.org/10.5194/egusphere-2026-2290
Preprint. Discussion started: 5 May 2026

References

Barlow, J., Halios, C., Lane, S., & Wood, C., 2015. Observations of urban boundary layer structure during a strong urban heat island event. Environmental Fluid Mechanics. 15, 373–398, https://doi.org/10.1007/s10652-014-9335-6

Che, J., & Zhao, P., 2021. Characteristics of the summer atmospheric boundary layer over the Tibetan Plateau and influential factors. Atmospheric Chemistry and Physics. 21(7), 5253–5268, https://doi.org/10.5194/acp-21-5253-2021

Chen, G., Zhang, X., & Fu, Y., 2022. Diurnal variation in clouds and radiative budgets over the Tibetan Plateau during summer using CERES data. Journal of Geophysical Research: Atmospheres. 127(16), e2021JD036329, https://doi.org/10.1029/2021JD036329

Chen, S., Hu, D., Wong, M., Ren, H., Cao, S., Yu, C., & Ho, H., 2019. Characterizing spatiotemporal dynamics of anthropogenic heat fluxes: A 20-year case study in Beijing–Tianjin–Hebei region in China. Environmental Pollution. 249, 923–931, https://doi.org/10.1016/j.envpol.2019.03.113

Chen, X., Škerlak, B., Rotach, M.W., Añel, J.A., Su, Z., Ma, Y., & Li, M., 2016. Reasons for the extremely high-ranging planetary boundary layer over the Tibetan Plateau. Journal of the Atmospheric Sciences. 73(5), 2021–2038, https://doi.org/10.1175/JAS-D-15-0148.1

Cheng, J., Zeng, Q., Sun, H., Yamin, G., Yang, F., Guo, M., & Wu, C., 2025. A global 1 km resolution daily surface longwave radiation product: Development and validation. Scientific Data. 12, Article 736, https://doi.org/10.1038/s41597-025-00736-8

Coll, C., Caselles, V., Valor, E., & Niclòs, R., 2012. Comparison between different sources of atmospheric profiles for land surface temperature retrieval from single channel thermal infrared data. Remote Sensing of Environment. 117, 199–210, https://doi.org/10.1016/j.rse.2011.09.018

Dessler, A., & Davis, S., 2010. Trends in tropospheric humidity from reanalysis systems. Journal of Geophysical Research: Atmospheres. 115(D19), D19127, https://doi.org/10.1029/2010JD014192

Feng, X., Wei, S., & Wang, S., 2020. Temperature inversions in the atmospheric boundary layer and lower troposphere over the Sichuan Basin, China: Climatology and impacts on air pollution. Science of The Total Environment. 726, 138579, https://doi.org/10.1016/j.scitotenv.2020.138579

Feng, X., Zhang, Z., Guo, J., & Wang, S., 2023. Multilayer inversion formation and evolution during persistent heavy air pollution events in the Sichuan Basin, China. Atmospheric Research. 286, 106691, https://doi.org/10.1016/j.atmosres.2022.106691

Galfi, V., & Lucarini, V., 2021. Fingerprinting heatwaves and cold spells and assessing their response to climate change using large deviation theory. Physical Review Letters. 127(5), 058701, https://doi.org/10.1103/PhysRevLett.127.058701

https://doi.org/10.5194/egusphere-2026-2290
Preprint. Discussion started: 5 May 2026

448 Gelaro, R., et al., 2017. The Modern-Era Retrospective Analysis for Research and Applications, Version 2 (MERRA-2). Journal
449 of Climate. 30(14), 5419–5454, https://doi.org/10.1175/JCLI-D-16-0758.1
450 Grimmond, C., et al., 2010. Climate and more sustainable cities: Climate information for improved planning and management
451 of cities (producers/capabilities perspective). Procedia Environmental Sciences. 1, 247–274,
452 https://doi.org/10.1016/j.proenv.2010.09.016
453 Guo, J., Chen, X., Su, T., Liu, L., Zheng, Y., Chen, D., Li, J., Xu, H., Lv, Y., He, B., Li, Y., Hu, X, Ding, A., & Zhai, P., 2020.
454 The climatology of lower tropospheric temperature inversions in China from radiosonde measurements: Roles of black carbon,
455 local meteorology, and large-scale subsidence. Journal of Climate. 33(21), 9327–9350, https://doi.org/10.1175/JCLI-D-19-
456 0278.1
457 Guo, J., Miao, Y., Zhang, Y., Liu, H., Li, Z., Zhang, W., He, J., Lou, M., Yan, Y., Bian, L., & Zhai, P., 2016a. The climatology
458 of planetary boundary layer height in China derived from radiosonde and reanalysis data. Atmospheric Chemistry and Physics.
459 16(20), 13309–13319, https://doi.org/10.5194/acp-16-13309-2016
460 Guo, J., Su, T., Li, Z., Miao, Y., Li, J., Liu, H., Xu, H., Cribb, M., & Zhai, P., 2016b. Declining frequency of summertime local-
461 scale precipitation over eastern China from 1970 to 2010 and its potential link to aerosols. Geophysical Research Letters.
462 44(11), 5700–5708, https://doi.org/10.1002/2017GL073533
463 Harris, I., Osborn, T., Joins, P., & Lister, D., 2020. Version 4 of the CRU TS monthly high-resolution gridded multivariate
464 climate dataset. Scientific Data. 7(1), 109, https://doi.org/10.1038/s41597-020-0453-3
465 He, G., et al., 2023. Nighttime ozone in the lower boundary layer: insights from 3-year tower-based measurements in South
466 China and regional air quality modeling. Atmospheric Chemistry and Physics. 23, 13107–13124, https://doi.org/10.5194/acp-
467 23-13107-2023
468 Hersbach, H., et al., 2020. The ERA5 global reanalysis. Quarterly Journal of the Royal Meteorological Society. 146(730),
469 1999–2049, https://doi.org/10.1002/qj.3803
470 Huang, F., Zhan, W., Wang, Z.H., Voogt, J., Hu, L., Quan, J., Liu, C., Zhang, N., & Lai, J., 2020. Satellite identification of
471 atmospheric surface subsurface urban heat islands under clear sky. Remote Sensing of Environment. 250, 112039,
472 https://doi.org/10.1016/j.rse.2020.112039
473 Huang, G., Chen, Y., Li, Z., Liu, Q., Wang, Y., He, Q., Liu, T., Liu, X., Zhang, Y., Gao, J., & Yao, Y., 2020. Validation and
474 accuracy analysis of the Collection 6.1 MODIS aerosol optical depth over the westernmost city in China based on Sun–Sky
475 Radiometer observations from SONET. Earth and Space Science. 7(2), e2019EA001041,
476 https://doi.org/10.1029/2019EA001041
477 Huang, Q., Chu, Y., & Li, Q., 2021. Climatology of low-level temperature inversions over China based on high-resolution

https://doi.org/10.5194/egusphere-2026-2290
Preprint. Discussion started: 5 May 2026

radiosonde measurements. Theoretical and Applied Climatology. 144(1–2), 415–429, https://doi.org/10.1007/s00704-021-03536-w

Kaushal, S., Singh, D., & Sreenivas, K., 2022. Penetrative convection in nocturnal atmospheric boundary layer and radiation fog. arXiv preprint. arXiv:2209.13185, https://arxiv.org/abs/2209.13185

King, M.D., Menzel, W.P., Kaufman, Y.J., Tanré, D., Gao, B.C., Platnick, S., Ackerman, S.A., Remer, L.A., Pincus, R., & Hubanks, P.A., 2003. Cloud and aerosol properties, precipitable water, and profiles of temperature and water vapor from MODIS. IEEE Transactions on Geoscience and Remote Sensing. 41(2), 442-458.

Leng, P., Liao, Q., Gao, M., Duan, S., Li, Z., Zhang, X., & Shang, G., 2019. A full satellite-driven method for the retrieval of clear-sky evapotranspiration. Earth and Space Science. 6(12), 2251–2262, https://doi.org/10.1029/2019EA000869

Li, H., Liu, B., Gong, W., Ma, Y., Jin, S., Wang, W., Fan, R., & Jiang, S., 2025. Influence of clouds on planetary boundary layer height: A comparative study and factors analysis. Atmospheric Research. 314, 107784, https://doi.org/10.1016/j.atmosres.2024.107784

Li, J., Chen, H., Li, Z., Wang, P., Fan, X., He, W., & Zhang, J., 2019. Analysis of low-level temperature inversions and their effects on aerosols in the lower atmosphere. Advances in Atmospheric Sciences. 36(11), 1235–1250, https://doi.org/10.1007/s00376-019-9018-9

Li, Y., Thompson, D., Stephens, G., & Bony, S., 2014. A global survey of the instantaneous linkages between cloud vertical structure and large-scale climate. Journal of Geophysical Research: Atmospheres. 119(7), 3770–3792, https://doi.org/10.1002/2013JD020669

Liu, B., Ma, X., Ma, Y., Li, H., Jin, S., Fan, R., & Gong, W., 2022. The relationship between atmospheric boundary layer and temperature inversion layer and their aerosol capture capabilities. Atmospheric Research. 271, 106121, https://doi.org/10.1016/j.atmosres.2022.106121

Luo, Y., Wang, S., Zhang, L., Tian, B., Jia, J., Sun, W., Wu, X., Ding, M., & Zuo, Z., 2025. Comparative evaluation of reanalysis-derived temperature profiles and low-level temperature inversion on the Tibetan Plateau. Research in Cold and Arid Regions, https://doi.org/10.1016/j.rcar.2025.08.004

Ma, Y., Huang, X., Yang, X., Li, Y., Wang, Y., & Liang, T., 2023. Mapping snow depth distribution from 1980 to 2020 on the Tibetan Plateau using multi-source remote sensing data and downscaling techniques. ISPRS Journal of Photogrammetry and Remote Sensing. 205, 246–262, https://doi.org/10.1016/j.isprsjprs.2023.10.012

Meier, R., Davin, E., Bonan, G., Lawrence, D., Hu, X., Duveiller, G., Prigent, C., & Seneviratne, S., 2022. Impacts of a revised surface roughness parameterization in the Community Land Model 5.1. Geoscientific Model Development. 15(6), 2365–2393, https://doi.org/10.5194/gmd-15-2365-2022

https://doi.org/10.5194/egusphere-2026-2290
Preprint. Discussion started: 5 May 2026

508 Ning, G., Wang, S., Yim, S., Li, J., Hu, Y., Shang, Z., Wang, J., & Wang, J., 2018. Impact of low-pressure systems on winter
509 heavy air pollution in the northwest Sichuan Basin, China. Atmospheric Chemistry and Physics. 18(19), 13601–13615,
510 https://doi.org/10.5194/acp-18-13601-2018
511 Platnick, S., King, M., Ackerman, S., Menzel, W., Baum, B., Riedi, J., & Frey, R., 2003. The MODIS cloud products:
512 Algorithms and examples from Terra. IEEE Transactions on Geoscience and Remote Sensing. 41(2), 459–473,
513 https://doi.org/10.1109/TGRS.2002.808301
514 Saha, S., et al., 2010. The NCEP Climate Forecast System Reanalysis. Bulletin of the American Meteorological Society. 91(8),
515 1015–1057, https://doi.org/10.1175/2010BAMS3001.1
516 Santer, B., et al., 2018. Human influence on the seasonal cycle of tropospheric temperature. Science. 361(6399), eaas8806,
517 https://doi.org/10.1126/science.aas8806
518 Schwarz, N., Lautenbach, S., & Seppelt, R., 2011. Exploring indicators for quantifying surface urban heat islands of European
519 cities with MODIS land surface temperatures. Remote Sensing of Environment. 115(12), 3175–3186,
520 https://doi.org/10.1016/j.rse.2011.07.003
521 Seeley, J., & Wordsworth, R., 2021. Episodic deluges in simulated hothouse climates. Nature. 599(7883), 74–79,
522 https://doi.org/10.1038/s41586-021-03919-z
523 Seemann, S., Borbas, E., Li, J., Menzel, W., & Gumley, L., 2006. MODIS Atmospheric Profile Retrieval Algorithm Theoretical
524 Basis Document (Version 6). Cooperative Institute for Meteorological Satellite Studies, University of Wisconsin–Madison,
525 Madison, WI, https://modis-images.gsfc.nasa.gov/_docs/MOD07_atbd_v7_April2011.pdf
526 Seidel, D.J., Li, J., Mears, C., Moradi, I., Nash, J., Randel, W.J., Saunders, R., Thompson, D.W.J., & Zou, C.Z., 2016.
527 Stratospheric temperature changes during the satellite era. Journal of Geophysical Research: Atmospheres. 121(2), 664-681.
528 Sobrino, J., Jiménez-Muñoz, J., Mattar, C., & Sòria, G., 2014. Evaluation of Terra/MODIS atmospheric profiles product
529 (MOD07) over the Iberian Peninsula: A comparison with radiosonde stations. International Journal of Remote Sensing. 35(3),
530 771–783, https://doi.org/10.1080/01431161.2013.873153
531 Song, Z., Bai, W., Zhang, Y., Wang, Y., Xu, X., & Xin, J., 2024. Evaluation of satellite-derived atmospheric temperature and
532 humidity profiles and their application as precursors to severe convective precipitation. Remote Sensing. 16(24), 4638,
533 https://doi.org/10.3390/rs16244638
534 Tan, J., Che, T., Wang, J., Liang, J., Zhang, Y., & Ren, Z., 2021. Reconstruction of the daily MODIS land surface temperature
535 product using the two-step improved similar pixels method. Remote Sensing. 13(9), 1671, https://doi.org/10.3390/rs13091671
536 Thorne, P., Lanzante, J., Peterson, T., Seidel, D., & Shine, K., 2016. Tropospheric temperature trends: History of an ongoing
537 controversy. Wiley Interdisciplinary Reviews: Climate Change. 7(1), 51–67, https://doi.org/10.1002/wcc.398

https://doi.org/10.5194/egusphere-2026-2290
Preprint. Discussion started: 5 May 2026

538 Tian, Y., Ghausi, S., Zhang, Y., Zhang, M., Xie, D., Cao, Y., Mei, Y., Wang, G., Zhong, D., & Kleidon, A., 2023. Radiation as
539 the dominant cause of high-temperature extremes on the eastern Tibetan Plateau. Environmental Research Letters. 18(7),
540 074007, https://doi.org/10.1088/1748-9326/acd805
541 Xue, Y., Zhu, X., Wu, Z., & Duan, S., 2023. Retrieval of land surface temperature over mountainous areas considering terrain
542 effects. Remote Sensing. 15(23), 5465, https://doi.org/10.3390/rs15235465
543 Yuan, B., Li, X., Zhou, L., Bai, T., Hu, T., Huang, J., Liu, D., Li, Y., & Guo, J., 2023. Global distinct variations of surface
544 urban heat islands in inter- and intra-cities revealed by local climate zones and seamless daily land surface temperature data.
545 ISPRS Journal of Photogrammetry and Remote Sensing. 204, 1–14, https://doi.org/10.1016/j.isprsjprs.2023.08.012
546 Zeng, H., Tian, P., Zhang, M., Cao, X., Liang, J., & Zhang, L., 2022. Rapid change in surface-based temperature inversions
547 across the world during the last three decades. Journal of Applied Meteorology and Climatology. 61(2), 175–184,
548 https://doi.org/10.1175/JAMC-D-21-0093.1
549 Zhang, A., & Zhang, X., 2019. Landsat-8-based land surface temperature inversion and comparative analysis with MODIS
550 temperature product. Journal of Beijing Forestry University. 41(3), 1–13, https://doi.org/10.13332/j.1000-1522.20180234
551 Zhang, K., Zhao, L., Yang, K., Qin, J., Song, L., Ni, X., Fan, L., & Han, X., 2023. Spatiotemporal scales of precipitation in the
552 Central Tibetan Plateau identified by in-situ soil moisture observations. Journal of Hydrology. 626, 130319,
553 https://doi.org/10.1016/j.jhydrol.2023.130319
554 Zhang, W., Zhang, B., Zhu, W., Tang, X., Li, F., Liu, X., & Yu, Q., 2021. Comprehensive assessment of MODIS-derived near-
555 surface air temperature using wide elevation-spanned measurements in China. Science of The Total Environment. 800, 149535,
556 https://doi.org/10.1016/j.scitotenv.2021.149535
557 Zhang, W., Zhao, J., Zhu, W., Kong, Y., Wan, B., & Liao, Y., 2025. Comprehensive validation of MODIS-derived instantaneous
558 air temperature and daily minimum temperature at nighttime. Remote Sensing. 17(10), 1732,
559 https://doi.org/10.3390/rs17101732
560 Zhang, Y., Zhang, B., & Yang, N., 2022. Characteristics of temperature and humidity inversions based on high-resolution
561 radiosonde observations at three Arctic stations. Journal of Applied Meteorology and Climatology. 61(4), 415–428,
562 https://doi.org/10.1175/JAMC-D-21-0054.1
563 Zhao, L., Lee, X., Smith, R., & Oleson, K., 2014. Strong contributions of local background climate to urban heat islands.
564 Nature. 511(7508), 216–219, https://doi.org/10.1038/nature13462
565 Zhao, X., Liu, C., Yang, N., & Li, Y., 2020. Diurnal and seasonal variations of surface energy and CO_2 fluxes over a site in the
566 western Tibetan Plateau. Atmosphere. 11(3), 260, https://doi.org/10.3390/atmos11030260